An improved impermeable solid boundary scheme for Meshless Local Petrov-Galerkin method

Xinglin Pan[a], Yan Zhou[a,*], Ping Dong[a], Huabin Shi[b]

[a] *School of Engineering, University of Liverpool, Liverpool, L69 3BX, UK*

[b] State Key Laboratory of Internet of Things for Smart City and Department of Civil and Environmental Engineering, University of Macau, Avenida da Universidade, Taipa, Macao, China

Abstract

Meshless methods have become an essential numerical tool for simulating a wide range of flow-structure interaction problems. However, the way by which the impermeable solid boundary condition is implemented can significantly affect the accuracy of the results and computational cost. This paper develops an improved boundary scheme through a weak formulation for the boundary particles based on Pressure Poisson's Equation (PPE). In this scheme, the wall boundary particles simultaneously satisfy the PPE in the local integration domain by adopting the Meshless Local Petrov-Galerkin method with the Rankine source solution (MLPG_R) integration scheme (Ma, 2005b) and the Neumann boundary condition, i.e., normal pressure gradient condition, on the wall boundary which truncates the local integration domain. The new weak formulation vanishes the derivatives of the unknown pressure at wall particles and is discretized in the truncated support domain without extra artificial treatment. This improved boundary scheme is validated by analytical solutions, numerical benchmarks, and experimental data in the cases of patch tests, lid-driven cavity, flow over a cylinder and monochromic wave generation. Second-order convergent rate is achieved even for disordered particle distributions. The results show higher accuracy in pressure and velocity, especially near the boundary, compared to the existing boundary treatment methods that directly discretize the pressure Neumann boundary condition.

Keywords:

Wall boundary conditions, Weak formulation, Meshless local Petrov-Galerkin method, Flow around structures

1. Introduction

Meshless methods have been intensively developed, especially in coastal and ocean engineering, benefiting from the relief of mesh generation and its inherent capacity in dealing with large-deformed wave surfaces. Applications of meshless methods to ocean and coastal engineering were recently reviewed in Luo et a. (2021). Several meshless methods have been developed based on various algorithms for discretizing Navier-Stokes equation, e.g., diffusion element (DE) method (Nayroles et

al., 1992), element free Galerkin (EFG) method (Belytschko et al., 1994), smoothed particle hydrodynamics (SPH) method (Monaghan, 1994) and meshless local Petrov-Galerkin (MLPG) method (Atluri & Zhu, 1998). However, the solid boundary implementation, which plays a significant role in flow-structure interaction, remains less developed comparing to that for fluid particles, either requiring artificial terms or having a lower accuracy.

In the SPH method, mass and momentum equations are discretized over neighbour particles within a support domain using kernel functions. Pressure is either explicitly expressed by the equation of state treating the fluid weakly compressible (WCSPH) or implicitly solved by the Pressure Poisson Equation (PPE) as the incompressible condition is adopted (ISPH). Several wall boundary approaches have been developed in SPH, including the repulsive force approach (Monaghan, 1994; Monaghan & Kajtar, 2009; Shadloo & Yildiz, 2011; Monaghan & Mériaux, 2018), the image or ghost particle approach (Morris et al., 1997; Liu et al. 2012; Bierbrauer et al., 2009), the dynamic particle approach (Liu & Liu, 2003; Gómez-Gesteira & Dalrymple, 2004; Gong et al., 2009), and the semi-analytical approach (Kulasegaram et al., 2004). In the repulsive force approach, the wall boundary condition is imposed by applying the repulsive force on fluid particles approaching solid walls to prevent them from penetrating the boundaries. This approach is capable of dealing with complex geometries at the boundary, but errors can be introduced due to the kernel truncation near the boundaries (Fourtakas et al., 2019). It is also reported that, in the static fluid test, particles near the wall boundaries undergo spurious movement (Ferrand et al., 2013). In the image particle approach, extra particles are generated beyond the wall boundaries with prescribed physical quantities (e.g. pressure and density) the same as fluid particles. The velocities and positions of image and fluid particles are set to be symmetrical with respect to the tangent of the boundary. The image particle approach can effectively prevent non-physical behaviours (Leroy et al., 2014) and improve the overall accuracy (Hosseini & Feng, 2011). However, challenges still remain in generating and adopting those particles, especially for computational domains with complex geometries. Furthermore, the computational cost for this approach is considerable due to image particle generation and movement (Wang et al., 2016). The dynamic particle approach uses virtual particles fixed beyond the wall boundaries with flow properties obtained from neighbouring fluid particles through linear extrapolation (Chen, 2020). According to Wang et al. (2016), the problem related to boundary deficiency for virtual particles still exists and may lead to inaccurate results in solving the pressure field. The semi-analytical approach is proposed by introducing a renormalization factor for fluid particles close to the wall boundaries (Kulasegaram et al., 2004; Ferrand et al., 2013; Mayrhofer et al., 2015). This approach improves the interpolation accuracy at the wall boundaries, but the difficulties in applications for complex boundary geometries remain (Valizadeh & Monaghan, 2015).

As an alternative to the SPH method, another type of meshless method based on the Galerkin formulation, i.e., the meshless local Petrov-Galerkin (MLPG) method, has also been developed and widely applied. Different from the SPH method that directly discretizes the strong form of the PPE, this method takes integration over a local sub-domain which reduces the order of the pressure derivative in the PPE (Ma, 2005a). An state-of-the-art review of the MLPG method, including its correlation with other particle-based methods, has been carried out in Sriram & Ma (2021).

According to Ma (2005a), solid boundary treatment approaches in MLPG was initially based on the weak formulation of flow governing equations over the incomplete sub-domains of the boundary particles but was only applied to solve the potential flow (Atluri & Zhu, 1998) and inviscid flow with artificial stabilizing term to suppress spurious pressure (Lin & Atluri, 2001). When the MLPG method was extended to simulate non-linear waves (Ma, 2005a), the wall boundary condition was imposed by direct discretization of the pressure Neumann boundary condition instead of its weak formulation. This wall boundary treatment approach excludes artificial stabilizing terms and prevents fluid particles from penetrating the wall with flow viscosity considered. Three schemes for directly discretising Neumann boundary condition were compared in Zhou et al. (2008), including two in MPS with single and three layers of boundary particles (Koshizuka & Oka, 1996; Hibi & Yabushta, 2004; Zhang et al., 2006) and one in MLPG based on simplified finite-difference interpolation (SFDI) (Ma, 2008). It was found that SFDI enabled more stable and accurate simulations. However, such an approach does not have a consistent weak formulation throughout the simulation domain. The flow governing equation near the boundary was not implemented at the particle distance scale. MLPG method was further improved by introducing the Rankine source solution (MLPG_R), instead of the Heaviside step function, as the test function for the fluid particles, in which the pressure derivative was entirely replaced by the pressure itself to be numerically solved (Ma, 2005b). The weak formulation for inner fluid particles in the MLPG_R improves the stability and accuracy in solving the PPE by entirely omitting Laplacian or gradient operator of the unknown pressure (Ma et al., 2016) and was successfully applied to problems such as 2D breaking waves (Ma & Zhou, 2009) and violent water waves (Zheng et al., 2014). As the treatment of wall boundary condition was unchanged with the gradient operator of the pressure being discretized directly, the errors introduced at the boundary can creep into the inner flow domain, especially in regions close to the solid walls.

In this work, using the local integration scheme of the MLPG_R method, a weak formulation for the wall boundary condition is developed that satisfies simultaneously the incompressible fluid governing equation in the local integration domain and the pressure Neumann boundary condition. The pressure gradient is eliminated for wall particles, leaving only the unknown pressure itself to be numerically discretized. The new formulation has been validated by the analytical solution of the patch

test with particles randomly distributed, numerical benchmarks of lid-driven cavity cases at various Reynolds numbers and monochronic waves. Validation on the curved boundary will also be carried out for flow over a cylinder in which pressure acting on the cylinder and wakes after the cylinder will be discussed.

2. Governing Equations

The governing equations are the incompressible and viscous Navier–Stokes equations in the Lagrangian form as follows:

$$\nabla \cdot \boldsymbol{u} = 0 \tag{1}$$

$$\frac{D\boldsymbol{u}}{Dt} = -\frac{1}{\rho}\nabla p + \boldsymbol{g} + v\nabla^2\boldsymbol{u} \tag{2}$$

where ρ is the density, which is a constant for the incompressible fluid, $\boldsymbol{u}$ is the velocity, $\boldsymbol{g}$ is the gravitational acceleration, p is the pressure, and v is the kinematic viscosity.

At the wall boundary, impermeability condition is applied by enforcing the normal component of the fluid velocity equals to that of the boundary velocity as

$$\boldsymbol{u} \cdot \boldsymbol{n} = \boldsymbol{U} \cdot \boldsymbol{n} \tag{3}$$

By substituting Eq. (3) into Eq. (2), the pressure at the wall satisfies

$$\boldsymbol{n} \cdot \nabla p = \rho(\boldsymbol{n} \cdot \boldsymbol{g} - \boldsymbol{n} \cdot \dot{\boldsymbol{U}} + v\boldsymbol{n} \cdot \nabla^2\boldsymbol{u}) \tag{4}$$

where $\boldsymbol{U}$ and $\dot{\boldsymbol{U}}$ are the velocity and the acceleration of the solid wall, respectively.

3. Numerical Method

3.1 Time marching procedure

The projection method solves pressure and velocity fields in many meshless simulations for incompressible fluids (Ma et al., 2016). Based on the known variables of each particle at n-th time step ($t = t_n$), intermediate velocity $\boldsymbol{u}^*$ and intermediate position $\boldsymbol{r}^*$ are explicitly calculated according to Eq. (2) without the pressure gradient term as

$$\boldsymbol{u}^* = \boldsymbol{u}^n + (v\nabla^2\boldsymbol{u}^n + \boldsymbol{g})\Delta t \tag{5}$$

$$\boldsymbol{r}^* = \boldsymbol{r}^n + \boldsymbol{u}^*\Delta t \tag{6}$$

By using the intermediate velocity and combining it with Eqs. (1) and (2), the pressure equation at t_{n+1} can be formulated as the Pressure Poisson Equation (PPE) as

$$\nabla^2 p^{n+1} = \frac{\rho}{\Delta t} \nabla \cdot \boldsymbol{u}^* \tag{7}$$

The PPE is numerically solved for both fluid particles as detailed in section 3.2 and for wall boundary particles with the impermeable wall boundary condition implemented in Section 3.3. Once the pressure field is obtained by solving Eq. (7), the velocity and position of the fluid particles can be updated by

$$\boldsymbol{u}^{n+1} = \boldsymbol{u}^* + \left(-\frac{1}{\rho}\nabla p^{n+1}\right)\Delta t \tag{8}$$

$$\boldsymbol{r}^{n+1} = \boldsymbol{r}^n + \boldsymbol{u}^{n+1}\Delta t \tag{9}$$

It should be noted that the velocity and position updates with Eqs. (8) and (9) are not applied on wall boundary particles as their velocity and position follow the movement of the wall boundaries by adopting either the non-slip or slip condition.

(a)   (b)

$(\partial\Omega_K = \partial\Omega_h \cup \partial\Omega_{b1+b2} \cup \partial\Omega_\varepsilon)$
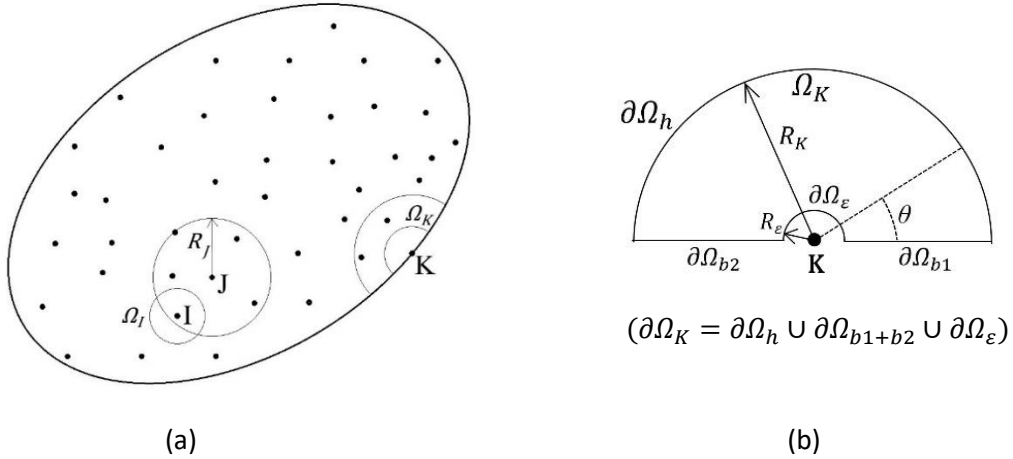
Figure 1. (a) Local sub-domain Ω_I for fluid particles I, support domain for fluid particle J with a radius of R_J and two domains for wall boundary particle K. (b) Demonstration of sub-domain for the wall boundary particle K, which is a semi-circle with the centre semi-circle Ω_ε, having the radius of R_ε, being taken out.

3.2 MLPG_R formulation for fluid particles

For fluid particles, such as node **I** and **J**, as demonstrated in Fig. 1(a), the weak formulation for numerical discretization involves the integration of PPE over local sub-domains as

$$\int_{\Omega_I} \left(\nabla^2 p^{n+1} - \frac{\rho}{\Delta t}\nabla \cdot \boldsymbol{u}^*\right) \varphi \, d\Omega = 0 \tag{10}$$

where φ is the test function and Ω_I is the integration sub-domain that can be of any arbitrary shape (Atluri & Shen, 2002). In the developed MLPG_R method (Ma, 2005b), the circular sub-domain with

the radius of $R_I = 0.8 \times \Delta l$ is adopted, where Δl is the initial particle distance. The test function adopted here is

$$\varphi = \frac{1}{2\pi} ln\left(\frac{r}{R_I}\right) \tag{11}$$

where r is the distance away from particle I, since the weak formulation is only applied on fluid particles, the integration sub-domain is entirely located in the fluid domain forming a complete circle. The test function φ satisfies $\nabla^2\varphi = 0$ in Ω_I and $\varphi = 0$ on its circular boundary of $\partial\Omega_I$. By applying Gauss's theorem to Eq. (10), the final weak formulation for fluid particles yields:

$$\int_{\partial\Omega_I} \boldsymbol{n} \cdot (p\nabla\varphi)\, dS - p = \int_{\Omega_I} \frac{\rho}{\Delta t} \boldsymbol{u}^* \cdot \nabla\varphi\, d\Omega \tag{12}$$

where $\partial\Omega_I$ is the boundary of Ω_I which is a complete circular curve, and $\boldsymbol{n}$ is the normal vector of the sub-domains pointing to the outside. For more details of the derivation of Eq. (12), readers are referred to Ma (2005b).

3.3 MLPG_R formulation for wall particles

In this study, instead of direct discretization of the impermeable wall boundary condition involving normal pressure gradient as in the previous MLPG_R method (Ma, 2005b), a new weak formulation will be derived for wall particles based on the PPE with impermeability condition of Eq. (3) imposed. As shown in Fig. 1(b), the sub-domain for the wall particle, K, is a semi-circle. By adopting the same test function as for the fluid particles, a zero term $p\nabla^2\varphi$ is added to the left-hand side of the PPE and then integrated over the sub-domain Ω_K. To apply Gauss's theory and to avoid the singularity of the test function at the centre of the sub-domain, a semi-circle with a radius being R_ε is extracted from the sub-domain and the integration becomes

$$\int_{\Omega_K} [(\nabla^2 p)\varphi - p\nabla^2\varphi]\, d\Omega = \int_{\partial\Omega_K} [\boldsymbol{n} \cdot (\varphi\nabla p) - \boldsymbol{n} \cdot (p\nabla\varphi)]\, dS \tag{13}$$

where $\partial\Omega_K$ is the boundary of the sub-domain consisting of a semi-circular boundary $\partial\Omega_h$, a flat boundary $\partial\Omega_b = \partial\Omega_{b1} \cup \partial\Omega_{b2}$ representing the wall boundary, and a semi-circular boundary $\partial\Omega_\varepsilon$ for avoiding the singularity at the centre, which will be taken as infinitesimal in the following derivation.

By taking $R_\varepsilon \to 0$, the first term of the right-hand side of Eq.(13), can be expressed as

$$\int_{\partial\Omega_h + \partial\Omega_b + \partial\Omega_\varepsilon} [\boldsymbol{n} \cdot (\varphi\nabla p)]\, dS = \int_{\partial\Omega_b} [\boldsymbol{n} \cdot (\varphi\nabla p)]\, dS \tag{14}$$

as it can be easily proven that

$\int_{\partial\Omega_h} [\boldsymbol{n} \cdot (\varphi\nabla p)]\, dS = 0$ as φ vanishes on $\partial\Omega_h$ and

$$\int_{\partial\Omega_\varepsilon} (\boldsymbol{n}\cdot\nabla p)\frac{1}{2\pi}\ln\left(\frac{r}{R_K}\right)dS = \int_0^{\boldsymbol{\pi}} (\boldsymbol{n}\cdot\nabla p)\frac{1}{2\pi}\ln\left(\frac{R_\varepsilon}{R_K}\right)R_\varepsilon\, d\theta = 0 \text{ as } \lim_{R_\varepsilon\to 0} ln\left(\frac{R_\varepsilon}{R_K}\right)R_\varepsilon = 0$$

And the second term can be manipulated to become

$$\int_{\partial\Omega_h+\partial\Omega_b+\partial\Omega_\varepsilon}[\boldsymbol{n}\cdot(p\nabla\varphi)]\, dS = \int_{\partial\Omega_h}[\boldsymbol{n}\cdot(p\nabla\varphi)]\, dS - \frac{p}{2} \tag{15}$$

as

$$\int_{\partial\Omega_\varepsilon}\boldsymbol{n}\cdot(p\nabla\varphi)\, dS = -\frac{p}{2} \text{ and}$$

$$\int_{\partial\Omega_b}[\boldsymbol{n}\cdot(p\nabla\varphi)]\, dS = 0$$

Combining Eq. (14) and (15) gives the weak formulation of the Laplacian pressure as

$$\int_{\Omega_K}(\nabla^2 p)\varphi\, d\Omega \;=\; \int_{\partial\Omega_b}\boldsymbol{n}\cdot(\varphi\nabla p)\, dS + \frac{p}{2} - \int_{\partial\Omega_h}[\boldsymbol{n}\cdot(p\nabla\varphi)]\, dS \tag{16}$$

Gauss theory is also applied to the integration of the term associated with the divergence of the intermediate velocity, and it reads

$$\int_{\Omega_K}\frac{\rho}{\Delta t}\varphi(\nabla\cdot\boldsymbol{u}^*)\, d\Omega = \int_{\Omega_K}\frac{\rho}{\Delta t}\nabla\cdot(\varphi\boldsymbol{u}^*)\, d\Omega - \int_{\Omega_K}\frac{\rho}{\Delta t}\boldsymbol{u}^*\cdot\nabla\varphi\, d\Omega$$

$$= \int_{\partial\Omega_b}\frac{\rho}{\Delta t}\boldsymbol{n}\cdot(\varphi\boldsymbol{u}^*)dS - \int_{\Omega_K}\frac{\rho}{\Delta t}\boldsymbol{u}^*\cdot\nabla\varphi\, d\Omega \tag{17}$$

in which the integration over the sub-domain boundary $\partial\Omega_K$ is reduced to $\partial\Omega_b$ as $\int_{\partial\Omega_h}\frac{\rho}{\Delta t}\boldsymbol{n}\cdot$ $(\varphi\boldsymbol{u}^*)dS = 0$ and $\int_{\partial\Omega_\varepsilon}\frac{\rho}{\Delta t}\boldsymbol{n}\cdot(\varphi\boldsymbol{u}^*)dS = 0$. Combining Eqs. (16) and (17), the final weak formulation for the wall boundary particles is expressed as

$$\int_{\partial\Omega_b}\boldsymbol{n}\cdot(\varphi\nabla p)\, dS + \frac{p}{2} - \int_{\partial\Omega_h}[\boldsymbol{n}\cdot(p\nabla\varphi)]\, dS \;=\; \int_{\partial\Omega_b}\frac{\rho}{\Delta t}\boldsymbol{n}\cdot(\varphi\boldsymbol{u}^*)dS - \int_{\Omega_K}\frac{\rho}{\Delta t}\boldsymbol{u}^*\cdot\nabla\varphi\, d\Omega \tag{18}$$

In Eq. (18), the first terms at the left- and right-hand sides are integrals over the boundary $\partial\Omega_b$, where the pressure Neumann condition satisfies. Thus Eq. (4) in the format of $\boldsymbol{n}\cdot\nabla p = \frac{\rho}{\Delta t}\boldsymbol{n}\cdot(\boldsymbol{u}^* - \boldsymbol{U})$ (Ma & Zhou, 2009) is implemented, and the two terms involving pressure gradient and intermediate velocity are vanished. The final formulation for the wall boundary particles yields

$$\int_{\partial\Omega_h}[\boldsymbol{n}\cdot(p\nabla\varphi)]\, dS - \frac{p}{2} = \int_{\Omega_K}\frac{\rho}{\Delta t}\boldsymbol{u}^*\cdot\nabla\varphi\, d\Omega - \int_{\partial\Omega_b}\frac{\rho}{\Delta t}\boldsymbol{n}\cdot(\varphi\boldsymbol{U})dS \tag{19}$$

For the scenarios that only involve fixed or tangentially moving boundaries, i.e., $\boldsymbol{n}\cdot\boldsymbol{U} = 0$, Eq. (19) can be further simplified as

$$\int_{\partial\Omega_h}[\boldsymbol{n}\cdot(p\nabla\varphi)]\,dS - \frac{p}{2} = \int_{\Omega_K}\frac{\rho}{\Delta t}\boldsymbol{u}^*\cdot\nabla\varphi\,d\Omega \tag{20}$$

This new formulation for wall particles satisfies the PPE in the local sub-domain and has the impermeable wall boundary condition implemented for both fixed and moving walls. Furthermore, because all terms involving derivatives of the unknown pressure are removed, the accuracy and efficiency of solving for pressure at the wall boundary can be much improved to the same level as for fluid particles (Ma, 2005a, b).

It should be noted that the semi-circular sub-domain used in the derivation assumes that the wall boundary truncating the sub-domain is a straight line and is the diameter of the sub-domain. This can be justified by the fact that the size of the sub-domain is small with the same scale of the particle distance, and the error induced by the assumption, when applied to curved boundaries, can be reduced by increasing the number of particles on the boundary. Simulations of flow over a cylinder will be presented in Section 4.3, in which the proposed scheme will be applied on curved wall boundary with various particle distances tested.

3.4 Discretized Equations

For fluid and wall particles governed by the weak formulations of Eqs. (12) and (19) respectively, the unknown pressure will be approximated by a set of neighbouring particles and discretized as

$$p(\boldsymbol{x_i}) \approx \sum_{j=1}^{N}\Phi_j(\boldsymbol{x})\hat{p}_j \tag{21}$$

where Φ_j is the interpolation function in terms of neighbour particle j which is located within the support domain of particle i and will be formulated by the Moving Least Square (MLS) method in this paper, which is detailed in Belytschko et al. (1994) and Atluri et al. (1999), N is the total number of neighbour particles affecting the pressure at $\boldsymbol{x}$, and $\hat{p}_j$ is the pressure of each neighbour particle.

In this paper, the size of supporting domain is chosen to be $1.85 \times \Delta l$ as it was taken in the MLPG_R method (Ma, 2005b), where Δl is the initial particle distance. The linear equation set for pressures of all the particles with the total number of n, $\boldsymbol{P} = [p_1, p_2, \dots p_n]$, is written as

$$\boldsymbol{SK}\cdot\boldsymbol{P} = \boldsymbol{FB} \tag{22}$$

where

$$\boldsymbol{SK}_{ij} = \begin{cases} \int_{\partial\Omega_I}\Phi_j(\boldsymbol{x_i})\boldsymbol{n}\cdot\nabla\varphi\,dS - \Phi_j(\boldsymbol{x_i}) & \text{fluid particles} \\ \int_{\partial\Omega_h}\Phi_j(\boldsymbol{x_i})\boldsymbol{n}\cdot(\nabla\varphi)\,dS - \frac{\Phi_j(\boldsymbol{x_i})}{2} & \text{wall particles} \end{cases} \tag{23}$$

$$FB_i = \begin{cases} \int_{\Omega_I} \frac{\rho}{\Delta t} \boldsymbol{u}^* \cdot \nabla \varphi \, d\Omega & \text{fluid particles} \\ \int_{\Omega_K} \frac{\rho}{\Delta t} \boldsymbol{u}^* \cdot \nabla \varphi \, d\Omega - \int_{\partial \Omega_b} \frac{\rho}{\Delta t} \boldsymbol{n} \cdot (\varphi \boldsymbol{U}) dS & \text{wall particles} \end{cases} \quad (24)$$

By keeping the same formulation for the fluid particles, the direct discretization of the wall boundary condition, as in Ma & Zhou (2009), is presented in Eqs. (25) and (26) for comparison, which shows that the newly developed weak formulation removes the gradient approximation for the unknown pressure. The derivation process also fulfils the mass and momentum conservation and the impermeable wall condition.

$$SK_{ij} = \boldsymbol{n} \cdot \nabla \Phi_j(\boldsymbol{x}_i) \quad (25)$$

$$FB_i = \frac{\rho}{\Delta t} \boldsymbol{n} \cdot (\boldsymbol{u}^* - \boldsymbol{U}) \quad (26)$$

In Eq. (23), for terms involving line integration over $\partial \Omega_I$ and $\partial \Omega_h$ for fluid and boundary particles, respectively, Gaussian quadrature is adopted for each quarter segment of the circular integration surface by using two Gaussian points (Ma, 2005b). Domain integration of explicitly calculated intermediate velocity will be carried out for fluid and wall particles. As for the intermediate velocity calculation in Eq. (5), the viscous term involving velocity Laplacian is obtained by the second-order MLS method. Alternative Laplacian operators such as QSFDI and CSPM are discussed in Korzilius et al. (2016), Yan et al. (2020) and Zhang et al. (2021). Several numerical techniques are developed for the integral evaluation, such as the classic Gaussian quadrature method (Atluri et al., 1999; Sellountos & Polyzos, 2003) and the semi-analytical method (Ma, 2005b). The Gaussian quadrature method is relatively time-consuming for domain integration due to the required number of Gaussian points, e.g., 16 points for 2D simulation. Recently a more efficient integration technique was developed for 3D simulation with only 6 points needed and quantified the order of the error (Agarwal et al., 2021, Sriram and Ma, 2021). In this study, the domain integration technique follows that proposed in Ma (2005b), dividing the domain into four divisions and requiring 4 points in total, which is sufficiently efficient for 2D simulations. Similar to Agarwal et al. (2021), it assumes the field values (i.e., intermediate velocities) have a linear variation over each division for the analytical integration. As discussed in 3.2 and 3.3, the domain integration for fluid particles is over a complete circle while it is over a semi-circle for a single layer of the wall particles. Once Eq. (22) is solved and the pressure field is obtained, velocity and particle position updates will be explicitly carried out according to Eq. (8) and (9) with the SFDI scheme (Ma, 2008) adopted for pressure gradient estimation.

4. Model Validations

In this section, four test cases, namely patch test for solving Poisson's equation, lid-driven cavity, flow over a cylinder and monochromic wave generation, which have analytical solutions, numerical

benchmarks and experimental results, are presented to validate the proposed scheme for implementing the boundary condition. The MLPG_R method for modelling fluid particles, without the special boundary treatment approach, is well established in solving linear potential flow problems (Atluri & Zhu, 1998), non-linear water waves (Ma, 2005a), and more recently, contaminant transport problems (Boddula & Eldho, 2017) and wave-vegetation interaction problems (Divya et al., 2020).

4.1 Patch tests for solving Poisson's equation

To test the performance of different numerical schemes, patch tests for solving Poisson's equation with comparisons with the analytical solution are widely reported (Schwaiger, 2008; Lind et al., 2012 and Zheng et al., 2014). In this study, the equation of $\nabla^2 p = 0$ in the patch of $0 \leq x \leq 1$ and $0 \leq y \leq 1$ will be solved. Four solid boundary conditions are defined as $\frac{\partial p}{\partial x}\big|_{x=0} = 0, \frac{\partial p}{\partial x}\big|_{x=1} = 0, \frac{\partial p}{\partial y}\big|_{y=0} = 0$ and $\frac{\partial p}{\partial y}\big|_{y=1} = \pi \sinh(\pi y)\cos(\pi x)$ which lead to the analytical solution of $p(x, y) = \cosh(\pi y)\cos(\pi x)$.

The equation is numerically solved by the newly developed boundary condition scheme as well as the existing scheme involving direct discretization of the wall boundary condition (Ma, 2005a) for comparison. A range of particle distances Δl = 0.01, 0.0125, 0.01666, 0.025 and 0.05 in both x and y directions are tested corresponding to total particle numbers of 10201, 6561, 3721, 1681 and 441 respectively in the patch. To achieve the particle distribution similar to that in the real flow simulation, controlled randomness is added to regularly distributed particles with the coordinates modified by $\Delta l' = (1 + k(Rn - 0.5))\Delta l$ where Rn is a random number ranging from 0 to 1, and k is a constant for adjusting the disorderliness of the particles. The accuracy is quantified by evaluating the mean error for all particles as $Er = \sqrt{\sum |p_i - p_{i,a}|^2} / \sqrt{\sum |p_{i,a}|^2}$, where p_i is the numerically solved pressure and $p_{i,a}$ is the analytical solution.
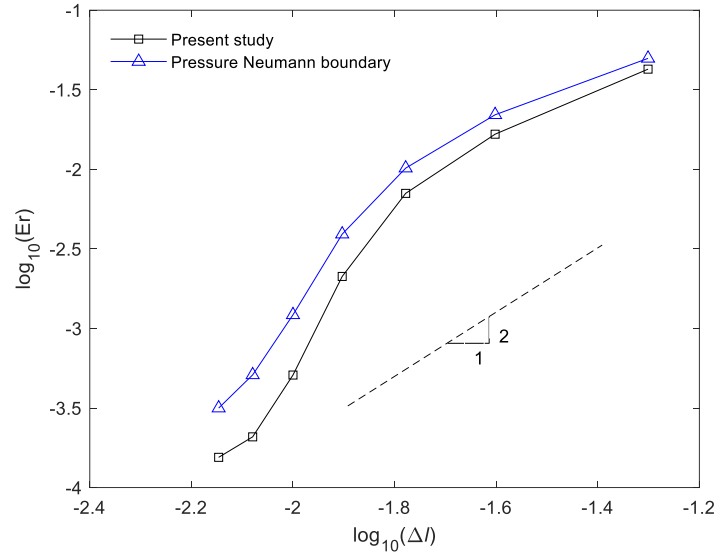
Figure 2. Errors of the new boundary scheme and direct discretisation of pressure Neumann boundary condition for different particle distances of Δl =0.007, 0.008, 0.01, 0.0125, 0.01666, 0.025, 0.05 with the randomness of $k = 0.3$. The dashed line is to indicate the 2:1 gradient.

Fig.2 shows the errors of numerical results using the direct discretization of the wall boundary condition by the SFDI scheme (Ma, 2008) and the present weak formulation. It can be seen that with different numbers of particles employed at typical randomness in the simulation $k = 0.3$, the errors of the new boundary scheme are smaller than those with the existing direct discretization scheme. The scheme also achieves overall second-order convergence for particle distance, as shown in Fig.2. When examining wall boundary particles only, the mean error for the particle distance of $\Delta l = 0.01m$ is 6.299×10^{-4} by adopting the new boundary approach, which is lower than 1.729×10^{-3} obtained by the direct discretisation approach. Since the numerical scheme remains the same for all the inner particles, the reduced mean errors, including all the particles as shown in Fig. 2, indicate that the improvement on the boundary condition implementation also significantly impacts the equation solving for the inner particles.
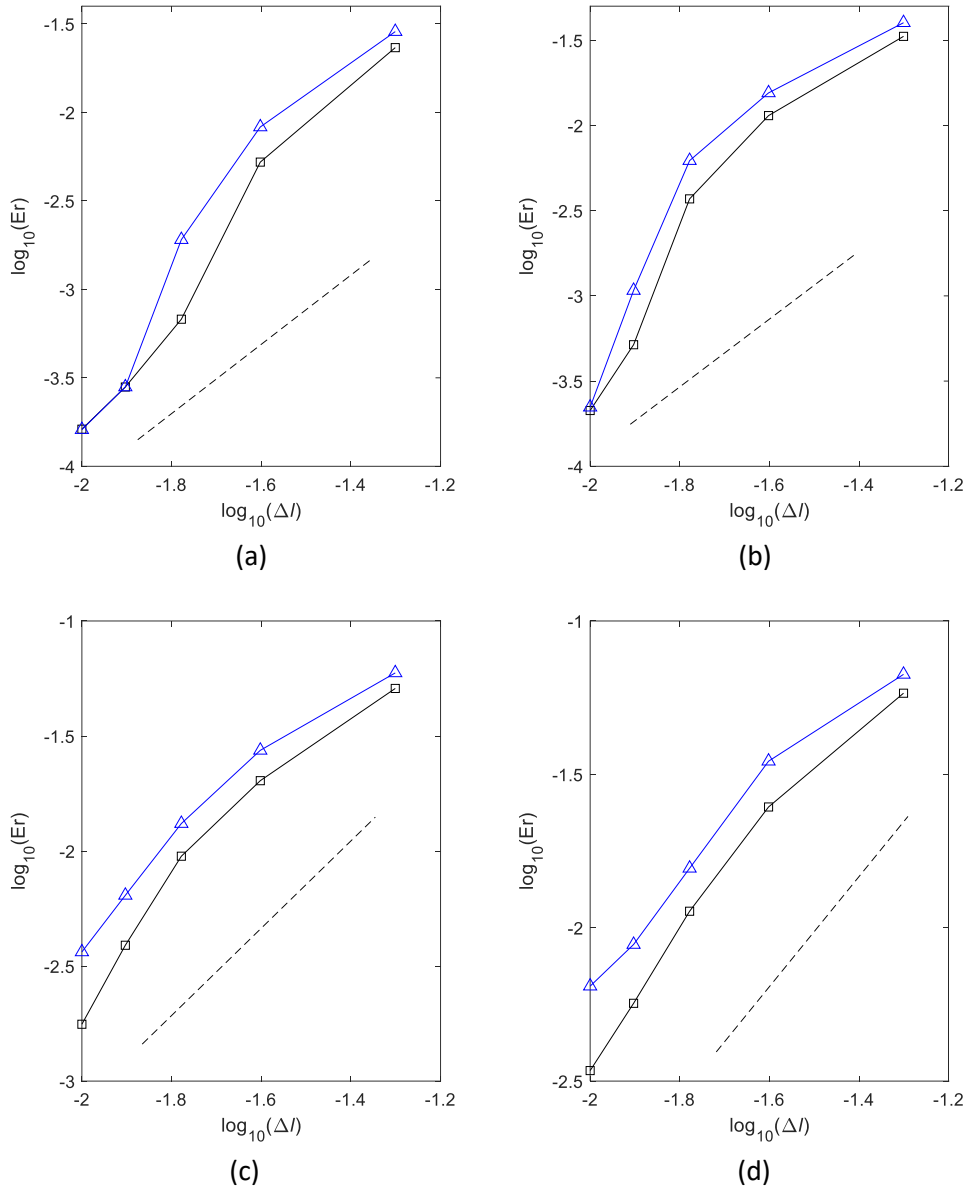
Figure 3. Errors of the direct Neumann boundary condition scheme (triangle markers) and the improved weak formulation boundary scheme (square marker) for different particle distances Δl =0.01, 0.0125, 0.01666, 0.025, 0.05 with different randomness in (a) $k = 0.1$, (b) $k = 0.2$, (c) $k = 0.4$ and (d) $k = 0.5$. The dash lines are to indicate the 2:1 gradient.

Further tests for the various particle distributions by ranging randomness k from 0.1 to 0.5 are carried out, and results are compared with the existing scheme as shown in Fig.3. For both schemes, errors slightly increase as the increased disorder is introduced in the distribution of particles, which is consistent with results from other meshless methods (Basic et al., 2018). It also can be seen that the new scheme shows better performance over the full range of randomness and particle distances. For minor disordered particles ($k = 0.1$ and 0.2), the performances of the two schemes are similar, especially when particle distance is sufficiently fine, i.e., $\Delta l = 0.01$, while for higher disordered distribution ($k = 0.4$ and 0.5), the new scheme achieves much higher accuracy.

In addition to the mean error, the number of particles having large errors, which may lead to simulation instability, is also investigated. For the case with $\Delta l = 0.01$ and $k = 0.3$, the maximum errors 1.534×10^{-2} and 2.424×10^{-2} for the new and existing schemes, respectively. Fig.4 shows the number of particles having large errors, which are higher than 20% of the maximum error in the simulation. Those particles are divided into groups with an increment of 10% relative to the maximum error. It can be seen that 97 particles out of 10201 in total have errors between 20% and 30% of the maximum error in the present scheme. While the number is doubled for the existing boundary condition scheme in this error range, and this is the case for all other larger error ranges.
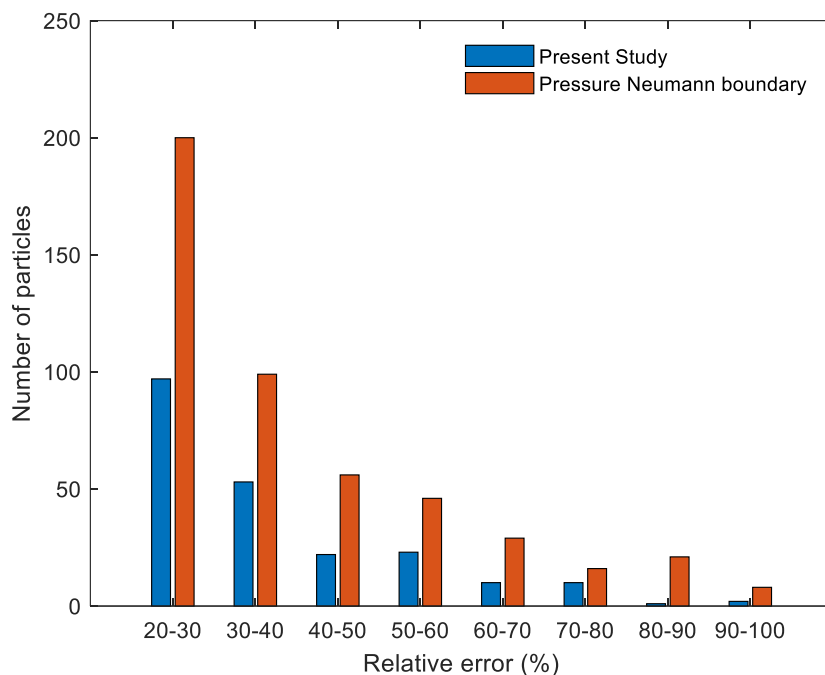
Figure 4. The number of particles, the blue column for the new scheme and the red column for the existing scheme, has errors within the ranges compared to the maximum error.

4.2 Lid-driven cavity

In this section, the lid-driven cavity flow in a 2D square domain with the length of sides being $L = 1m$ is considered. This case has been used to examine the accuracy and efficiency of other numerical methods such as the Finite Volume method (Ghia et al., 1982), which will be used as the benchmark. The flow in the rigid wall confined domain is driven by the lid sliding laterally at a constant velocity of $U_{lid} = 1m/s$. The flow regime is classified by Reynolds number defined as $Re = U_{lid}L/v$ where v denotes the kinematic viscosity of the fluid. Re from 100 to 3200 are tested, covering a wide range of the flow regime which can reach a steady state (Peng et al., 2003).

(a)   (b)
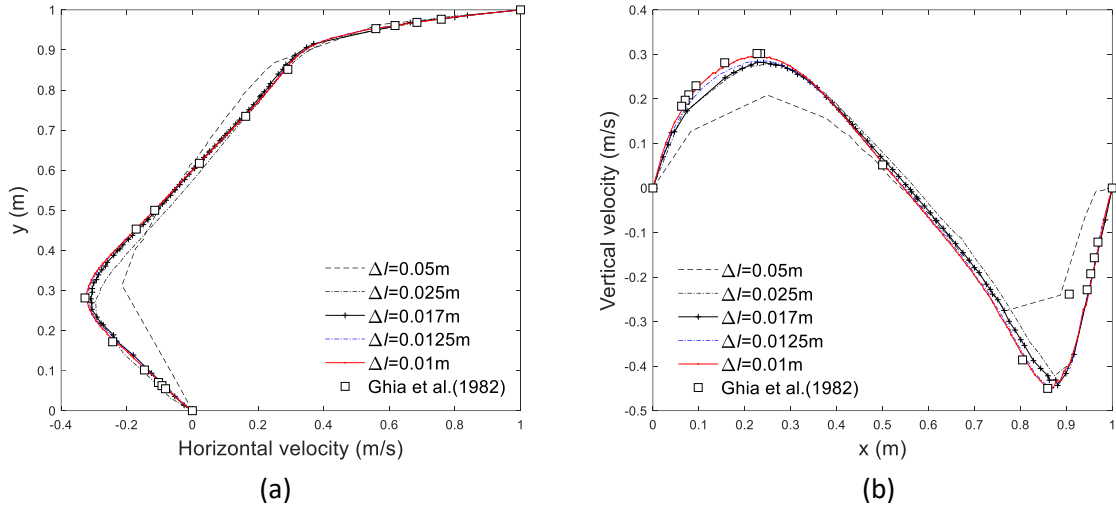
Figure 5. Velocities of lid-driven cavity flow at Re =400 obtained by the MLPG_R method with the new wall boundary scheme using different particle distances and the benchmark. (a) Horizontal velocity at x=L/2 and (b) Vertical velocity at y=L/2.

The convergence test regarding to the particle distance is firstly carried out for Re = 400 with Δl = 0.05m, 0.025m, 0.017m, 0.013m and 0.01m corresponding to total particle numbers of 21×21, 41×41, 61×61, 81×81 and 101×101 respectively. Horizontal and vertical velocities at x=L/2 and y=L/2 respectively, are plotted for all the resolutions along with the benchmark results (Ghia et al., 1982) as shown in Fig.5. It can be seen that with the particle number increased, both velocities gradually approach the benchmark with the results from 81×81 well agreed with the benchmark. To ensure the accuracy of the simulations, particle distance $\Delta l = 0.01$ (corresponding to the particle number of 101×101) will be adopted for the following cases unless stated otherwise.

The velocities for the flows with Re being from 100 to 3200 are plotted and compared with those simulated by the existing boundary condition scheme in Fig.6. The results of the new boundary condition scheme show good agreement with those in Ghia et al. (1982) across the whole range of the Re. Similar performance of both schemes at low $Re = 100$ as shown in Fig. 6(a) and (b) is to be expected due to the maximum velocities in flows with lower Re are developed far away from the boundaries, i.e., the magnitude of the horizontal velocity becomes maximum at $y = 0.5m$, and that happens at $x = 0.22m$ and $0.8m$ for the vertical velocity, which is less sensitive to the boundary treatment. When Re is increased, the improvement by the new boundary scheme becomes significant, especially for the maximum velocities which occur closer to the wall boundaries. As for the case of $Re = 1000$, the maximum horizontal velocity occurs at $y = 0.18m$, which is closer to the bottom boundary and that for the vertical velocity occurs at $x = 0.15m$ and 0.9m which move forward the two sidewalls. One should also note that when the Re is further increased to 3200, although the
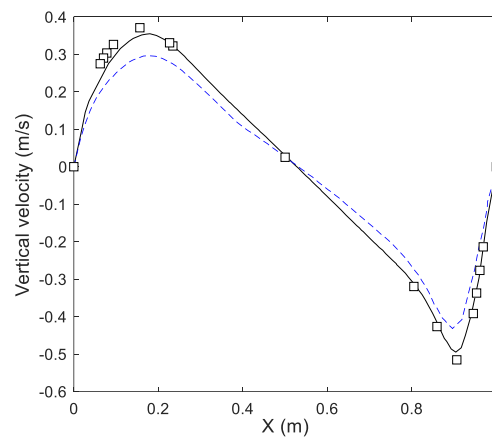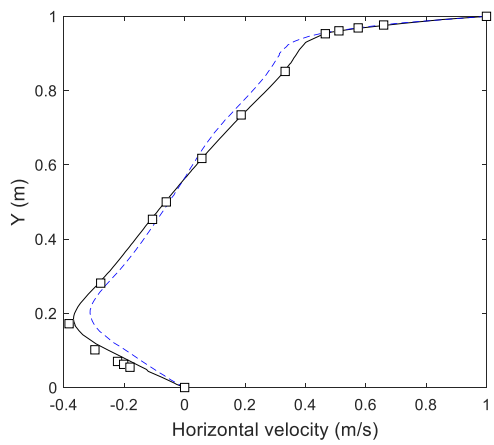
results are improved from the previous scheme, velocities are slightly underestimated may be caused by the lack of consideration for turbulence which is not the focus of this paper.
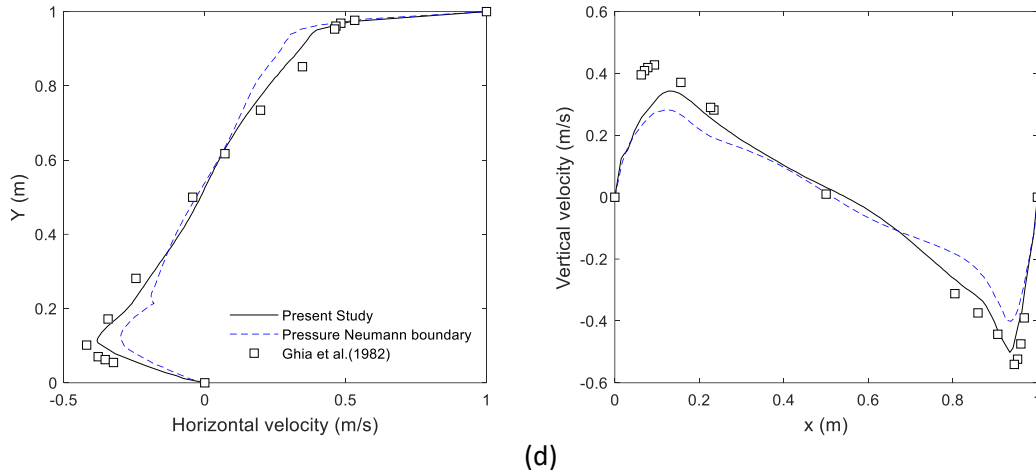

(a)

(b)

(c)

(d)
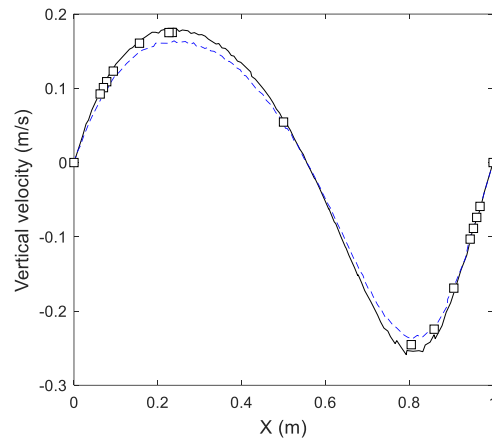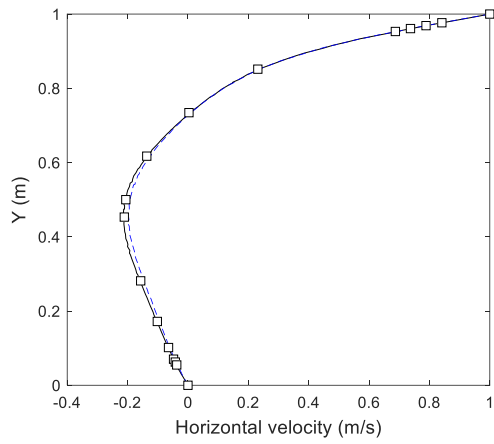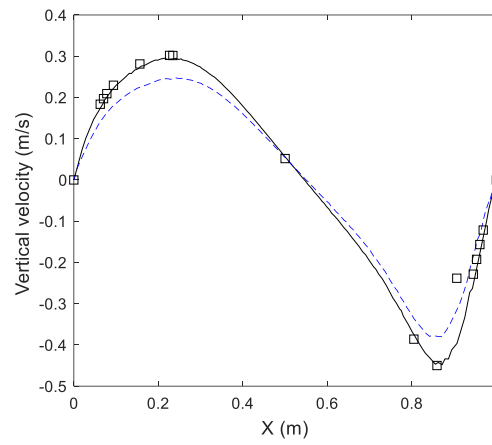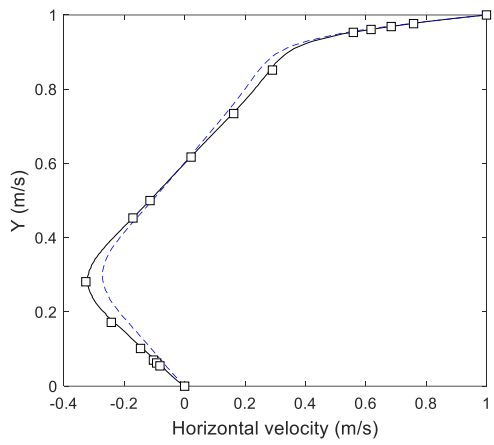
Figure 6. Velocities of the lid-driven cavity flow by adopting the improved wall boundary scheme (solid black line) and the existing wall boundary scheme (blue dash line). (a) to (d) are results of $Re = 100$, 400, 1000 and 3200 with horizontal velocities at $x = L/2$ in the left column and vertical velocities at $y = L/2$ in the right column. The squares are benchmarks from the Finite Volume Method (Ghia et al., 1982).

4.3 Flow over a cylinder

In this section, simulations are carried out for flow over a cylinder to show the capacity of the new boundary scheme for handling curved boundaries. As shown in Fig.7, flow with a constant inlet velocity u_a=0.1m/s interacting with a cylinder is simulated in a rectangular domain with the length of L=0.9m and the height of H=0.6m. The cylinder has a radius of R=0.02m and is located at x=0.5m and y=0.3m. The Reynolds number of the flow is defined by $Re = u_a 2R/v$.

To simulate continuous inflow and outflow at two ends of the channel, the periodic boundary condition is applied by returning the particles to the inlet once it reaches the outlet. It is achieved by setting multiple layers of particles, with the width of $W = 0.1$m, in the inlet and outlet zone to be mirrored to the outside of the domain by carrying all the flow properties. This treatment also completes the support domains for particles at inlet and outlet boundaries.
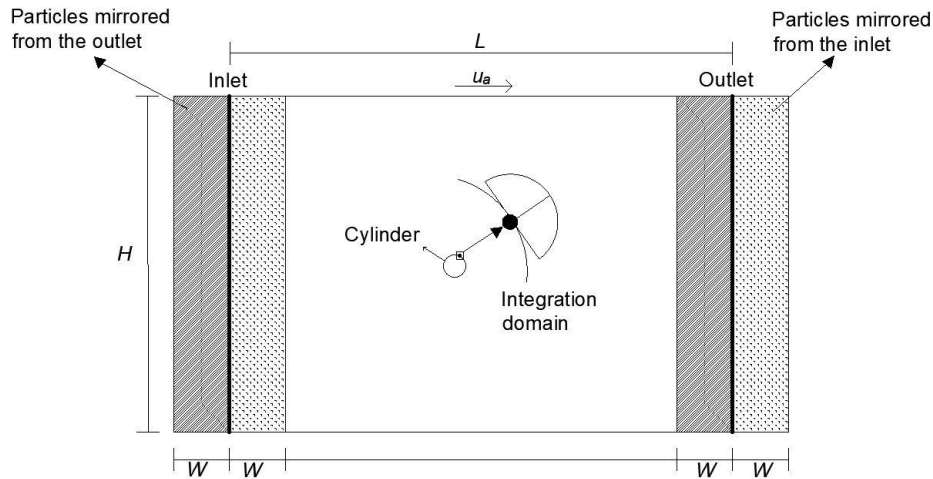
Figure 7. Illustration of the simulation domain with mirrored particles to achieve periodic boundaries and integration domain tangent to the curved wall.

The new boundary scheme is applied on all the solid boundaries, including the top wall, bottom wall, and cylinder surface. To use the semi-circular sub-domain on the wall particles at the curved boundary, the diameter goes through the wall particle and tangents to the curved wall, as illustrated in Fig.7. It is worth noting that the wall boundary condition is applied on the diameter of the semi-circle as that for the flat boundary rather than on the actual surface of the cylinder. The error induced by this procedure can be reduced by increasing the number of particles which has been tested by setting the different particle numbers distributed at the circular wall boundary with $\Delta l = 2\pi R/12$, $2\pi R/18$, $2\pi R/24$ and $2\pi R/30$. The flow with $Re = 40$ is simulated, and the pressures relative to the far-field pressure around the cylinder surface are shown in Fig.8. It can be seen that the results converge at $\Delta l = 2\pi R/24 \approx 0.005m$ and show a negligible difference when the particle distance is further decreased to $\Delta l = 2\pi R/30$. Therefore, the particle distance of $\Delta l = 2\pi R/24$ will be adopted for other flow over cylinder tests.
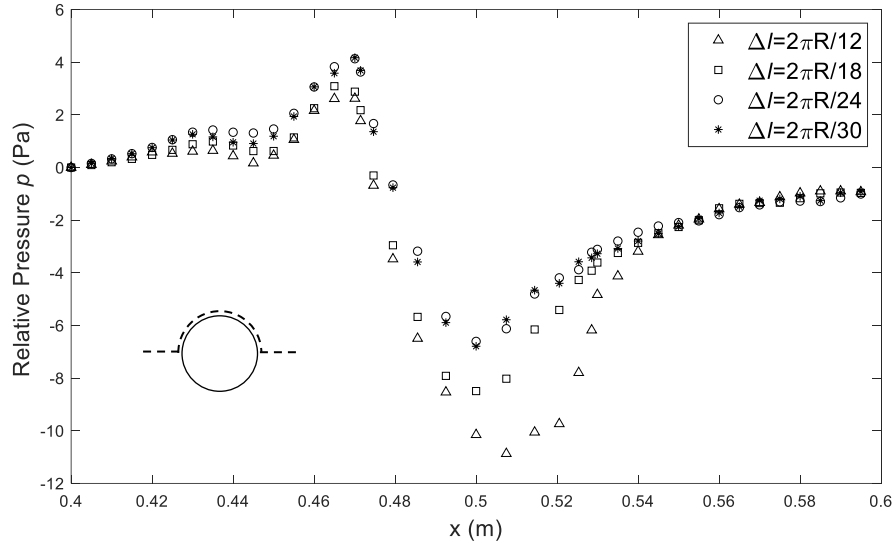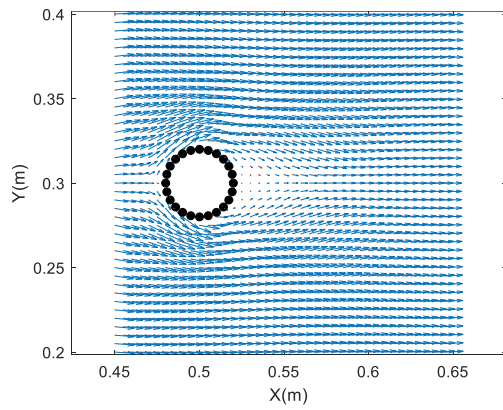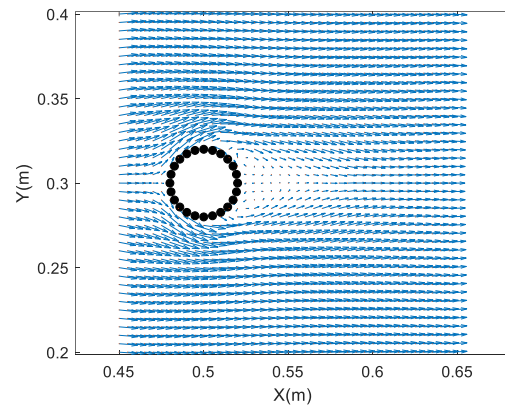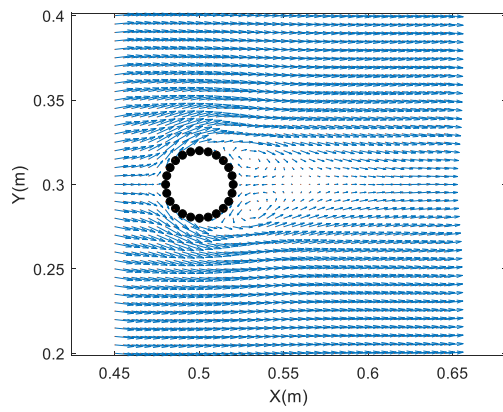
Figure 8. Pressure distribution along the upper half surface of the cylinder as shown by dash line for different particle distances in the flow of $Re = 40$.
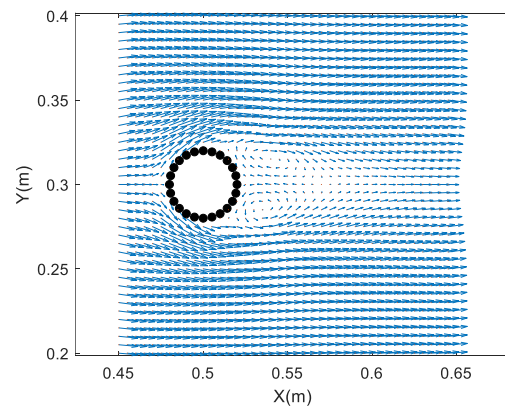

(a) Re =20

(b) Re =30

(c) Re =40

(d) Re =50

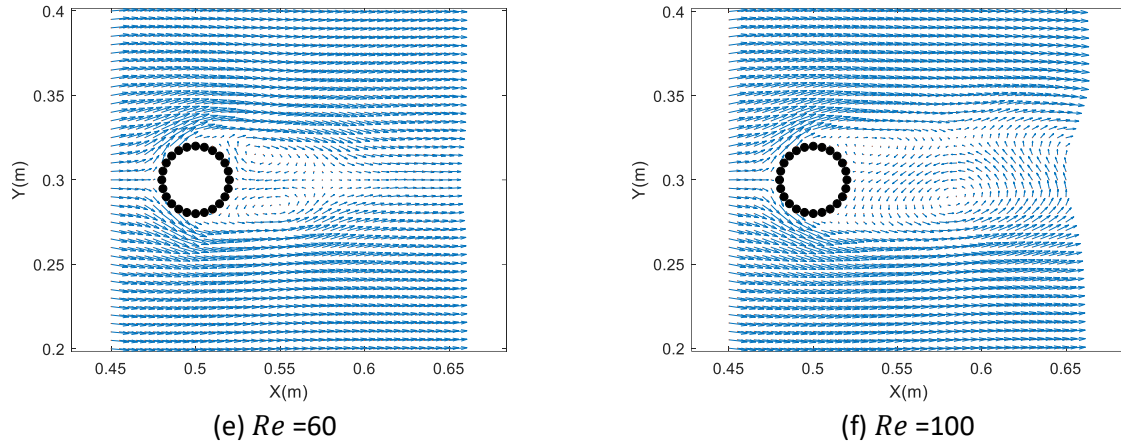(e) Re =60   (f) Re =100

Figure 9. Velocity field near the cylinder at (a) $Re = 20$; (b) $Re = 30$; (c) $Re = 40$; (d) $Re = 50$; (e) $Re = 60$ and (f) $Re = 100$.
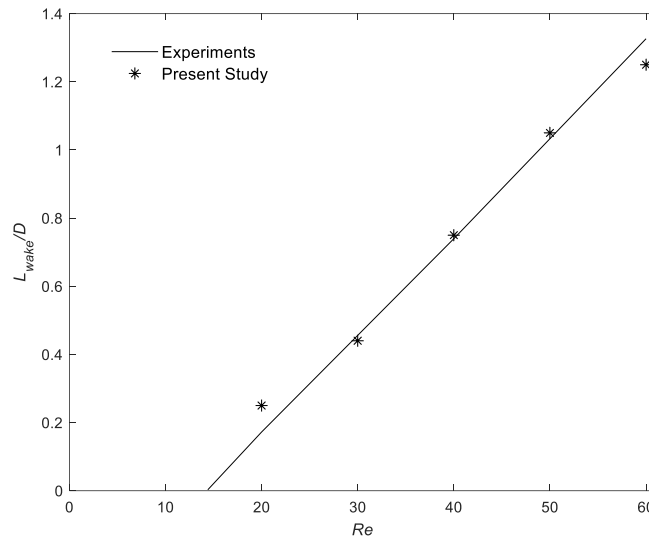

Figure 10. Comparison of normalized wake lengths L_{wake}/D with the experimental data (Coutanceau & Bouard, 1977).

The velocity fields are plotted in Fig. 9 for Re = 20, 30, 40, 50, 60 and 100. Complex flow phenomena near the cylindrical wall boundary involving wake flow, flow separation and vortex shedding are well captured by the new boundary scheme. It can be seen from Fig.9 (a) to (e) that two symmetrical vortexes are generated behind the cylinder for low Re up to 60, with the wake length increased when the Reynolds number gets higher. At a higher $Re = 100$, as shown in Fig. 10(f), non-symmetrical wakes are captured, which is consistent with the observation in Ding et al. (2004). Fig.10 demonstrates a good agreement between calculated and measured (Coutanceau & Bouard, 1977) wake lengths for various Re values. Furthermore, the distribution of time-averaged relative pressure coefficient $C_p = (p - p_\infty)/\frac{1}{2}\rho u_\infty^2$ along the upper half surface of the cylinder at $Re = 100$ is calculated, where p_∞ and u_∞ are the far-field pressure and velocity. Fig.11 shows a good agreement between the results

from the present model with the numerical results of Park et al. (1998), which used a high-resolution finite volume method. It should also be noted that the direct discretisation approach for the boundary condition is also tested with the same settings as that in the new boundary approach. Without using any regularization, particle disorder at the wake of the cylinder is significant, which leads to stability issues. But this is much improved for the new boundary scheme as the void in the wake of the cylinder was fairly small (the largest particle distance is about $1.3 \times \Delta l$) and do not expand throughout the simulation until equilibrium vortex is developed.
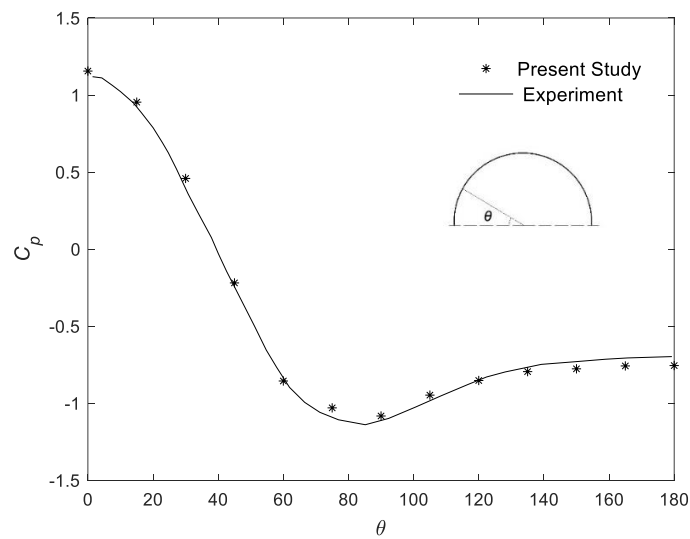

Figure 11. Comparison of the time-averaged pressure coefficient C_p along the upper half surface of the cylinder with experimental data (Park et al., 1998) at $Re = 100$.

### 4.4 Monochromic wave generation

In this section, the monochromic wave will be generated by a piston moving wavemaker to examine the performance of the proposed boundary scheme for the moving boundary with accelerations. The monochromic wave is generated in a long rectangular tank with water depth $H = 1m$ and tank length $L = 30m$, which is sufficiently long to contain several waves without reflection from the end of the tank. The motion of the wavemaker is governed by

$$S(t) = a(1 - \cos \omega t) \tag{27}$$

$$U_x(t) = a\omega \sin \omega t \tag{28}$$

where U_x is the velocity of the wavemaker in the wave progression direction with the amplitude $a = 0.01m$ and the frequency $\omega = 1.45s^{-1}$; S is the displacement of the wavemaker. Like the test in Zhou et al. (2008), the slip boundary condition is applied on the wavemaker with the tangential velocity obtained by calculating pressure gradient by the SFDI scheme. The generated waves have small wave

steepness, i.e., 0.012, and can be characterised as a linear wave for which the surface profile can be expressed by the linearized analytical solution (Eatock Taylor et al., 1994). By setting the initial particle distance $\Delta l = 0.04m$ and the time step $\Delta t = 0.02s$, the new boundary condition scheme is validated by the analytical solution by comparing wave profiles at two instants of $t = 24s$ and $t = 30s$ as shown in Fig.12. It can be seen that the present study has achieved a good agreement with the analytical solution, which demonstrates the capability of the proposed boundary scheme for treating moving boundaries.
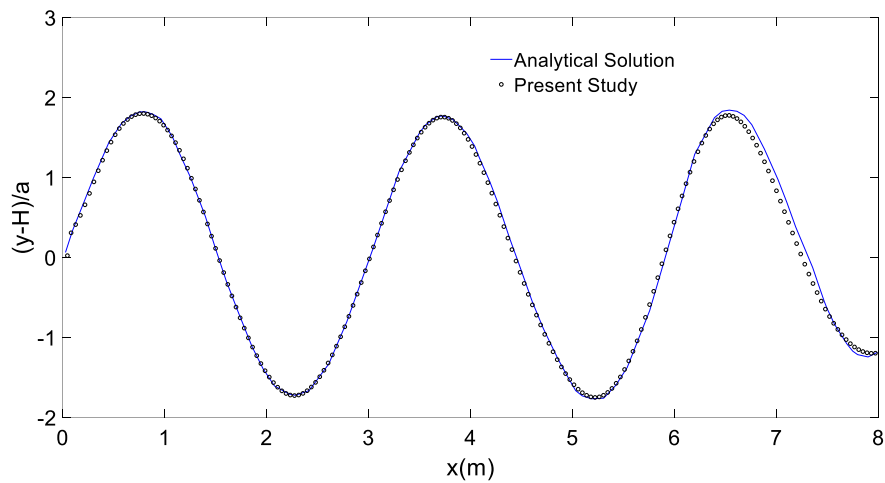
(a) $t = 24s$
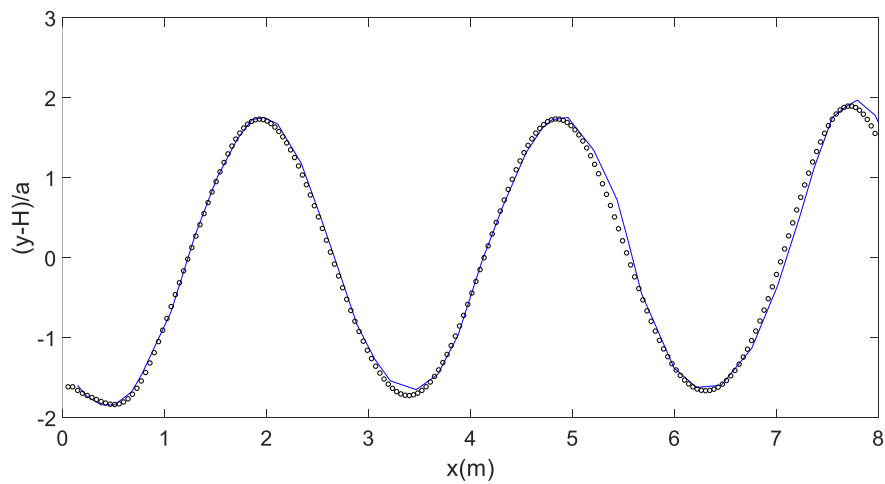
(b) $t = 30s$

Figure 12. Comparison with analytical solution (Eatock Taylor et al., 1994) of wave profiles at two instants (a) $t = 24s$ and (b) $t = 30s$ ($a = 0.01m$ and $\omega = 1.45s^{-1}$).

5. Conclusion

This study developed a new boundary condition implementation scheme for rigid and impermeable walls by integrating the PPE over a semi-circular sub-domain for wall boundary particles with the Neumann pressure boundary condition imposed. In this formulation, terms involving the derivative of the unknown pressure are removed to improve accuracy. Through validating the new scheme by the patch test of solving Poisson's equation, the new scheme achieves a second-order particle distance convergent rate for a range of disorderliness of particle distributions. Higher accuracy is also demonstrated by comparing the results with those of the previous scheme, which directly discretizes the pressure wall boundary condition, especially for particles with relatively high randomness through patch test validations. Apart from the reduction of mean error, the number of particles having large errors are also reduced, thus enhancing the stability of the simulation. In the lid-driven cavity cases, the velocity fields simulated by the model with the new boundary scheme has achieved good agreement with those by the well-established numerical method across a wide range of Reynolds number. The maximum velocities developed in the lid-driven cavity flow which appear near the wall boundary are better captured by the new boundary scheme. In the simulation of flow over a cylinder, the new boundary scheme is applied to the curved surface of the cylinder. The convergent results to various particle numbers show the capacity of the new scheme to deal with non-flat geometries. The development of symmetrical vortex and its length at low Reynolds number and asymmetrical vortex at high Reynolds number are all well captured compared with measurements. The capability of the new boundary approach is also validated for the moving boundary by generating monochromic waves using piston wavemaker as the wave surface profiles well agree with the analytical solutions.

Reference

Agarwal, S., Sriram, V., Yan, S., & Murali, K. (2021). Improvements in MLPG formulation for 3D wave interaction with fixed structures. *Computers and Fluids*, *218*.

Atluri, S. N., Kim, H. G., & Cho, J. Y. (1999). A critical assessment of the truly meshless local Petrov-Galerkin (MLPG), and local boundary integral equation (LBIE) methods. *Computational mechanics*, *24*(5), 348-372.

Atluri, S. N., & Shen, S. (2002). *The meshless method*. Encino, CA: Tech Science Press.

Atluri, S. N., & Zhu, T. (1998). A new meshless local Petrov-Galerkin (MLPG) approach in computational mechanics. *Computational mechanics*, *22*(2), 117-127.

Basic, J., Degiuli, N., & Ban, D. (2018). A class of renormalised meshless Laplacians for boundary value problems. *Journal of Computational Physics*, *354*, 269-287.

Belytschko, T., Lu, Y. Y., & Gu, L. (1994). Element-free Galerkin methods. *International journal for numerical methods in engineering*, *37*(2), 229-256.

Bierbrauer, F., Bollada, P. C., & Phillips, T. N. (2009). A consistent reflected image particle approach to the treatment of boundary conditions in smoothed particle hydrodynamics. *Computer Methods in Applied Mechanics and Engineering*, *198*(41-44), 3400-3410.

Boddula, S., & Eldho, T. I. (2017). A moving least squares based meshless local petrov-galerkin method for the simulation of contaminant transport in porous media. *Engineering Analysis with Boundary Elements*, *78*, 8-19.

Chen, F. (2020). Meshfree simulation of multiphase flows with SPH family methods. *arXiv preprint arXiv:2010.12189*.

Coutanceau, M., & Bouard, R. (1977). Experimental determination of the main features of the viscous flow in the wake of a circular cylinder in uniform translation. Part 1. Steady flow. *Journal of Fluid Mechanics*, *79*(2), 231-256.

Ding, H., Shu, C., Yeo, K. S., & Xu, D. (2004). Simulation of incompressible viscous flows past a circular cylinder by hybrid FD scheme and meshless least square-based finite difference method. Computer Methods in Applied Mechanics and Engineering, 193(9-11), 727-744.

Divya, R., Sriram, V., & Murali, K. (2020). Wave-vegetation interaction using Improved Meshless Local Petrov Galerkin method. *Applied Ocean Research*, *101*, 102116.

Ferrand, M., Laurence, D. R., Rogers, B. D., Violeau, D., & Kassiotis, C. (2013). Unified semi-analytical wall boundary conditions for inviscid, laminar or turbulent flows in the meshless SPH method. *International Journal for Numerical Methods in Fluids*, *71*(4), 446-472.

Fourtakas, G., Dominguez, J. M., Vacondio, R., & Rogers, B. D. (2019). Local uniform stencil (LUST) boundary condition for arbitrary 3-D boundaries in parallel smoothed particle hydrodynamics (SPH) models. *Computers & Fluids*, *190*, 346-361.

Ghia, U., Ghia, K. N., & Shin, C. T. (1982). High-Re solutions for incompressible flow using the Navier-Stokes equations and a multigrid method. *Journal of computational physics*, *48*(3), 387-411.

Gómez-Gesteira, M., & Dalrymple, R. A. (2004). Using a three-dimensional smoothed particle hydrodynamics method for wave impact on a tall structure. *Journal of waterway, port, coastal, and ocean engineering*, *130*(2), 63-69.

Gong, K., Liu, H., & Wang, B. L. (2009). Water entry of a wedge based on SPH model with an improved boundary treatment. *Journal of Hydrodynamics*, *21*(6), 750-757.

Hibi, S. & Yabushita, K. (2004). A study on reduction of unusual pressure fluctuation of MPS method. *J Kansai Soc NA Jpn*, *241*, 125-131.

Hosseini, S. M., & Feng, J. J. (2011). Pressure boundary conditions for computing incompressible flows with SPH. *Journal of Computational physics*, *230*(19), 7473-7487.

Korzilius, S. P., Schilders, W. H., & Anthonissen, M. J. (2016). An improved CSPM approach for accurate second-derivative approximations with SPH. *Journal of Applied Mathematics and Physics*, *5*(1), 168-184.

Koshizuka, S., & Oka, Y. (1996). Moving-particle semi-implicit method for fragmentation of incompressible fluid. *Nuclear science and engineering*, *123*(3), 421-434.

Kulasegaram, S., Bonet, J., Lewis, R. W., & Profit, M. (2004). A variational formulation based contact algorithm for rigid boundaries in two-dimensional SPH applications. *Computational Mechanics*, *33*(4), 316-325.

Leroy, A., Violeau, D., Ferrand, M., & Kassiotis, C. (2014). Unified semi-analytical wall boundary conditions applied to 2-D incompressible SPH. *Journal of Computational Physics*, *261*, 106-129.

Lin, H., & Atluri, S. N. (2001). The meshless local Petrov-Galerkin (MLPG) method for solving incompressible Navier-Stokes equations. *CMES- Computer Modeling in Engineering and Sciences*, *2*(2), 117-142.

Lind, S. J., Xu, R., Stansby, P. K., & Rogers, B. D. (2012). Incompressible smoothed particle hydrodynamics for free-surface flows: A generalised diffusion-based algorithm for stability and validations for impulsive flows and propagating waves. *Journal of Computational Physics*, *231*(4), 1499-1523.

Liu, G. R., & Liu, M. B. (2003). *Smoothed particle hydrodynamics: a meshfree particle method*. World scientific.

Liu, M., Shao, J., & Chang, J. (2012). On the treatment of solid boundary in smoothed particle hydrodynamics. *Science China Technological Sciences*, *55*(1), 244-254.

Luo, M., Khayyer, A., & Lin P. (2021). Particle methods in ocean and coastal engineering. *Applied Ocean Research 114,* 102734.

Ma, Q. W. (2005a). Meshless local Petrov–Galerkin method for two-dimensional non-linear water wave problems. *Journal of Computational Physics*, *205*(2), 611-625.

Ma, Q. W. (2005b). MLPG method based on Rankine source solution for simulating non-linear water waves. *CMES: Computer Modelling in Engineering &Sciences*, *9*(2), 193-209.

Ma, Q. W. (2008). A new meshless interpolation scheme for MLPG_R method. *CMES - Computer Modeling in Engineering and Sciences*, *23*(2), 75–89.

Ma, Q., & Zhou, J. (2009). MLPG_R method for numerical simulation of 2D breaking waves. *CMES: Computer Modeling in Engineering & Sciences*, *43*(3), 277-304.

Ma, Q. W., Zhou, Y., & Yan, S. (2016). A review on approaches to solving Poisson's equation in projection-based meshless methods for modelling strongly non-linear water waves. *Journal of Ocean Engineering and Marine Energy*, *2*(3), 279-299.

Mayrhofer, A., Ferrand, M., Kassiotis, C., Violeau, D., & Morel, F. X. (2015). Unified semi-analytical wall boundary conditions in SPH: analytical extension to 3-D. *Numerical Algorithms*, *68*(1), 15-34.

Monaghan, J. J. (1994). Simulating free surface flows with SPH. *Journal of computational physics*, *110*(2), 399-406.

Monaghan, J. J., & Kajtar, J. B. (2009). SPH particle boundary forces for arbitrary boundaries. *Computer physics communications*, *180*(10), 1811-1820.

Monaghan, J. J., & Mériaux, C. A. (2018). An SPH study of driven turbulence near a free surface in a tank under gravity. *European Journal of Mechanics-B/Fluids*, *68*, 201-210.

Morris, J. P., Fox, P. J., & Zhu, Y. (1997). Modeling low Reynolds number incompressible flows using SPH. *Journal of computational physics*, *136*(1), 214-226.

Nayroles, B., Touzot, G., & Villon, P. (1992). Generalizing the finite element method: diffuse approximation and diffuse elements. *Computational mechanics*, *10*(5), 307-318.

Park, J., Kwon, K., & Choi, H. (1998). Numerical solutions of flow past a circular cylinder at Reynolds numbers up to 160. *KSME international Journal*, *12*(6), 1200-1205.

Peng, Y. F., Shiau, Y. H., & Hwang, R. R. (2003). Transition in a 2-D lid-driven cavity flow. *Computers & Fluids*, *32*(3), 337-352.

Schwaiger, H. F. (2008). An implicit corrected SPH formulation for thermal diffusion with linear free surface boundary conditions. *International journal for numerical methods in engineering*, *75*(6), 647-671.

Sellountos, E. J., & Polyzos, D. (2003). A MLPG (LBIE) method for solving frequency domain elastic problems. *Computer Modeling in Engineering and Sciences*, *4*(6), 619-636.

Shadloo, M. S., & Yildiz, M. (2011). Numerical modeling of Kelvin–Helmholtz instability using smoothed particle hydrodynamics. *International Journal for Numerical Methods in Engineering*, *87*(10), 988-1006.

Sriram, V., & Ma, Q. W. (2021). Review on the local weak form-based meshless method (MLPG): Developments and Applications in Ocean Engineering. *Applied Ocean Research*, *116*(July).

Valizadeh, A., & Monaghan, J. J. (2015). A study of solid wall models for weakly compressible SPH. *Journal of Computational Physics*, *300*, 5-19.

Wang, Z. Bin, Chen, R., Wang, H., Liao, Q., Zhu, X., & Li, S. Z. (2016). An overview of smoothed particle hydrodynamics for simulating multiphase flow. *Applied Mathematical Modelling*, *40*(23–24), 9625–9655.

Yan, S., Ma, Q. W., & Wang, J. (2020). Quadric SFDI for Laplacian Discretisation in Lagrangian Meshless Methods. *Journal of Marine Science and Application*, *19*(3), 362-380.

Zhang, N., Yan, S., Ma, Q., & Zheng, X. (2021). A QSFDI based Laplacian discretisation for modelling wave-structure interaction using ISPH. *Applied Ocean Research*, *117*, 102954.

Zhang, S., Morita, K., Fukuda, K., & Shirakawa, N. (2006). An improved MPS method for numerical simulations of convective heat transfer problems. *International journal for numerical methods in fluids*, *51*(1), 31-47.

Zheng, X., Ma, Q. W., & Duan, W. Y. (2014). Incompressible SPH method based on Rankine source solution for violent water wave simulation. *Journal of Computational Physics*, *276*, 291-314.

Zhou, J. T., Ma, Q. W., & Yan, S. (2008). Numerical implementation of solid boundary conditions in meshless methods. *Proceedings of the International Offshore and Polar Engineering Conference*, *8*, 16–23.